Geophysical Journal International

Geophys. J. Int. (2020) **223,** 1100–1117
Advance Access publication 2020 August 05
GJI Seismology

doi: 10.1093/gji/ggaa366

Directionality of ambient noise in the Mississippi embayment

Chunyu Liu, Khurram Aslam and Charles A. Langston

Center for Earthquake Research and Information, University of Memphis, Memphis, TN 38152*, USA. E-mail: cliu5@memphis.edu*

Accepted 2020 July 26. Received 2020 July 23; in original form 2019 October 23

SUMMARY

Cross-correlations of ambient seismic noise from 277 broad-band stations within the Mississippi embayment (ME) with at least 1 month of recording time between 1990 and 2018 are used to estimate source locations of primary and secondary microseisms. We investigate source locations by analysing the azimuthal distribution of the signal-to-noise ratios (SNRs) and positive/negative amplitude differences. We use 84 stations with 1 yr of continuous recordings to explore seasonal variations of SNRs and amplitude differences. We also investigate the seasonal ambient noise ground motions using 2-D frequency–wavenumber (FK) analysis of a 50-station array. We observe that: (1) two major azimuths can be identified in the azimuthal distribution of SNRs and amplitude differences. We also observe two minor azimuths in the seasonal variation of SNRs, amplitude differences and 2-D FK power spectra. Monthly 2-D FK power spectra reveal that two energy sources are active in the Northern Hemisphere winter and two relatively weak sources are active in summer. (2) Backprojection suggests that primary microseisms originate along the coasts of Australia or New Zealand, Canada and Alaska, Newfoundland or Greenland and South America. (3) Secondary microseisms are generated in the deep water of the northern and southern Pacific Ocean, along the coasts of Canada and Alaska associated with near-shore reflections and in the deep water of south of Greenland. (4) Weak energy is observed in the third quadrant of the azimuthal distribution of amplitude differences of sedimentary Rayleigh and Love waves in the period band of 1–5 s and correlates with the direction of widening of the basin.

Key words: Seismic interferometry; Seismic noise; Wave scattering and diffraction.

1 INTRODUCTION

Ambient seismic noise in the short period band (1–20 s) is termed ‘microseisms’. Seismic noise with periods less than 5 s may be associated with anthropogenic activities (Lin *et al.* 2013; Nakata *et al.* 2015) or induced by basin edges (Joyner 2000; Rovelli *et al.* 2001). Noise with periods between 5 and 20 s is generated by different natural mechanisms (Wiechert 1904; Longuet-Higgins 1950; Hasselmann 1963). Primary (10–20 s) and secondary (5–10 s) microseisms are the two dominant types of noise in this band (Kibblewhite & Ewans 1985; Kedar *et al.* 2008). Primary microseisms are related to direct interaction of ocean swells with the ocean floor near coasts (Hasselmann 1963). Secondary microseisms are associated with the interaction between two primary ocean waves with the same frequency ranges but different propagation directions (Longuet-Higgins 1950). Numerical modelling of the generation of secondary microseisms suggests that the interaction can be in deep or shallow water (Ardhuin *et al.* 2011). In deep water, the interaction can be between wind-driven waves with a broad directional spectrum or two independent wave systems. In shallow water, the interaction can be between coastal reflections and the primary ocean wavefield (Ardhuin *et al.* 2011).

Under the assumption of uniformly distributed seismic noise sources, cross-correlation (CC) of continuous ambient noise recorded at two stations can effectively retrieve a Green’s function estimate between them (Weaver & Lobkis 2001; Derode *et al.* 2003; Snieder 2004; Wapenaar 2004). In the past decade, tomography using ambient noise CCs has been applied globally (Ritzwoller *et al.* 2002; Nishida *et al.* 2009), regionally (Yao *et al.* 2006; Lin *et al.* 2007, 2008; Liang & Langston 2008, 2009; Fu & Li 2015) and locally (Lin *et al.* 2013). Ambient noise tomography provides additional constraints on velocity structure for regions of active seismicity and sheds light on possible anomalous velocity structure for regions without local seismic sources. Ambient noise CCs can also be applied to monitor time-varying processes. Long-term monitoring of phase or arrival time differences of scattered waves in ambient noise CCs provides an opportunity to estimate possible seismic velocity changes in the crust. Estimating crustal velocity changes further advances our understanding of volcanic eruptions (Brenguier *et al.* 2008b; Duputel *et al.* 2009), fault zone co-seismic damage and post-seismic healing (Brenguier *et al.* 2008a; Wu *et al.* 2016; Liu *et al.* 2018b), crustal response to external loads such as precipitation (Sens-Schönfelder & Wegler 2006; Liu *et al.* 2020), temperature (Meier *et al.* 2010; Hillers

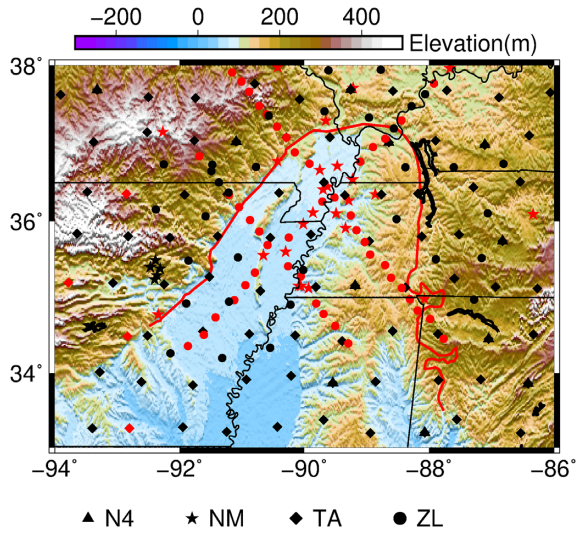

Figure 1. Index map of the Mississippi embayment in the central United States showing 277 broad-band stations installed in the period 1990–2018, the sediment boundary (a red solid line) modified from Dart (1992) and Dart & Swolfs (1998) and bedrock topography (Amante & Eakins 2009). Four networks, N4 (triangles), NM (stars), TA (diamonds) and ZL (circles), are used for the analysis of azimuthal distribution of SNRs and amplitude differences. 84 broad-band stations (red) had continuous recording in 2014 and are used for the investigation of seasonal variations of SNRs and amplitude differences.

et al. 2015) and atmospheric pressure (Silver *et al.* 2007; Niu *et al.* 2008).

Although ambient noise velocity and azimuthal anisotropy tomography methods provide an additional pathway for understanding Earth structure, they suffer from accuracy problems for regions without sufficient long-time recordings (Tsai 2009; Weaver *et al.* 2009; Yao & Van Der Hilst 2009; Harmon *et al.* 2010) because noise sources are usually heterogeneously distributed across the globe (Stehly *et al.* 2006; Yang & Ritzwoller 2008; Behr *et al.* 2013; Tian & Ritzwoller 2015). In the Northern Hemisphere, sources are distributed in the northern Pacific and Atlantic and the energy of sources varies seasonally from high energy in the winter to low in the summer (Young 1999). In the Southern Hemisphere, swells from storms occur throughout the Indian, Pacific and Atlantic Oceans; the energy of sources is high in Northern Hemisphere summer and low in winter. Thus, better knowledge of noise source distributions can help to assess the uncertainty of velocity tomography as well as understanding the mechanisms for noise generation.

As seen from North America, microseisms can originate from different locations and be related to different generation mechanisms. Source locations are rather complicated for the western United States. For secondary microseisms, seasonal variability of noise is weak and strong noise arrives from southwest quadrant, from the California coasts or from the deep Pacific Ocean (Yang & Ritzwoller 2008; Tian & Ritzwoller 2015). Strong seasonal variability can be observed for primary microseisms. In Northern Hemisphere winter, the strongest signals arrive from northwest and northeast quadrants, probably from the northern Pacific and Atlantic coasts of North America (Stehly *et al.* 2006; Gerstoft *et al.* 2008; Kedar *et al.* 2008; Landès *et al.* 2010; Retailleau *et al.* 2017) or near the southern tip of Greenland (Kedar *et al.* 2008). In northern summer, strong signals arrive from the south and southwest quadrants, from the California coasts (Yang & Ritzwoller 2008; Tian & Ritzwoller 2015). Source locations for primary and secondary microseisms in the eastern United States have been seen to have no significant differences. For primary and secondary microseisms, strong noise arrives from the northeast and west, from the coast of Newfoundland (Cessaro 1994; Langston *et al.* 2009) or Pacific coast of North America (Yang & Ritzwoller 2008). Microseisms can also be related to localized sources including rivers (Burtin *et al.* 2008) and lakes (Gu & Shen 2012).

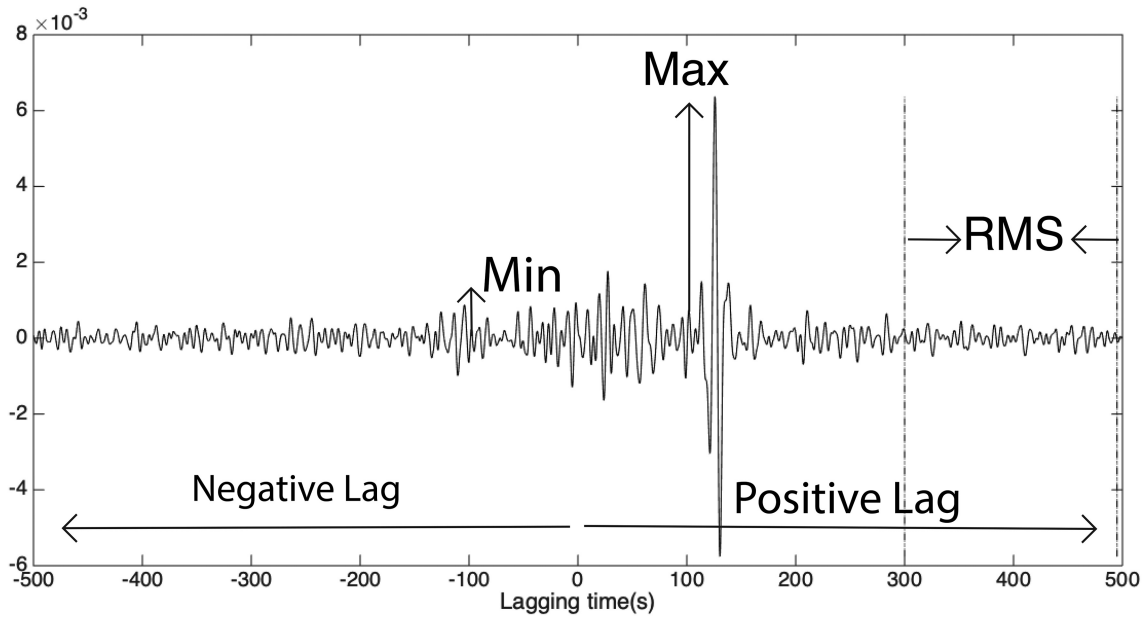

Figure 2. Illustration of the measurements of SNR and amplitude difference. The ZZ cross-correlation is between PENM of the New Madrid Cooperative Seismic Network and Z48A of EarthScope's Transportable array in the passband of 0.05–0.2 Hz. The peak amplitude is the maximum of the absolute velocity for positive time lags. The RMS is the root-mean-square value of the velocity marked between two dashed lines. Amplitude difference is the difference of maximum amplitude in positive and negative lags and is exaggerated 10 000 times for comparison with SNR measurements.

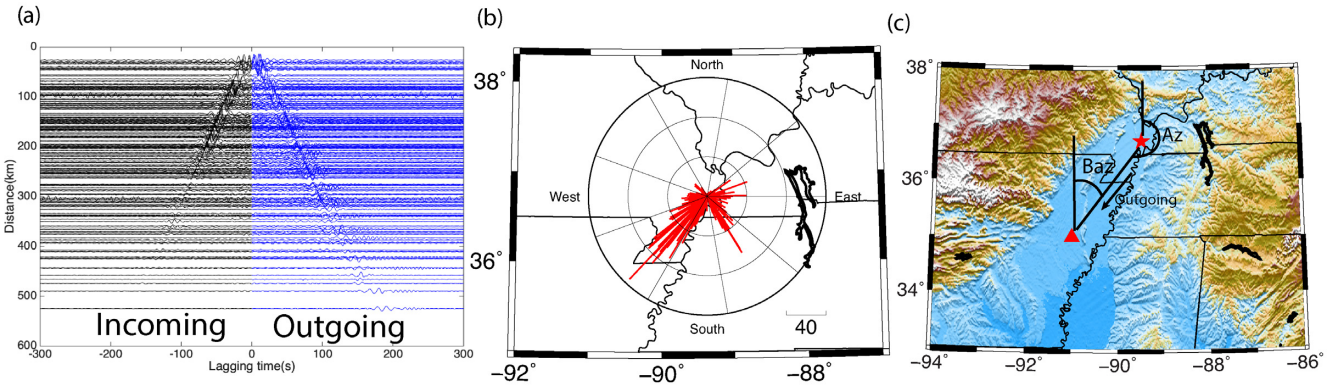

Figure 3. Construction of the SNR rose diagram. (a) CCs are for all surrounding stations relative to the virtual source HENM [red star in panel (c)]. Positive lags of CCs correspond to the outgoing wave from the virtual source. (b) Each bar represents one SNR measurement on an outgoing wave between two stations. The length of the bar indicates the magnitude of the SNR measurement. The rose diagram is made by collecting all of the SNR measurements. Note the scale length of 40 for each contour on the rose plot. (c) Azimuth and backazimuth definition for rose diagrams.

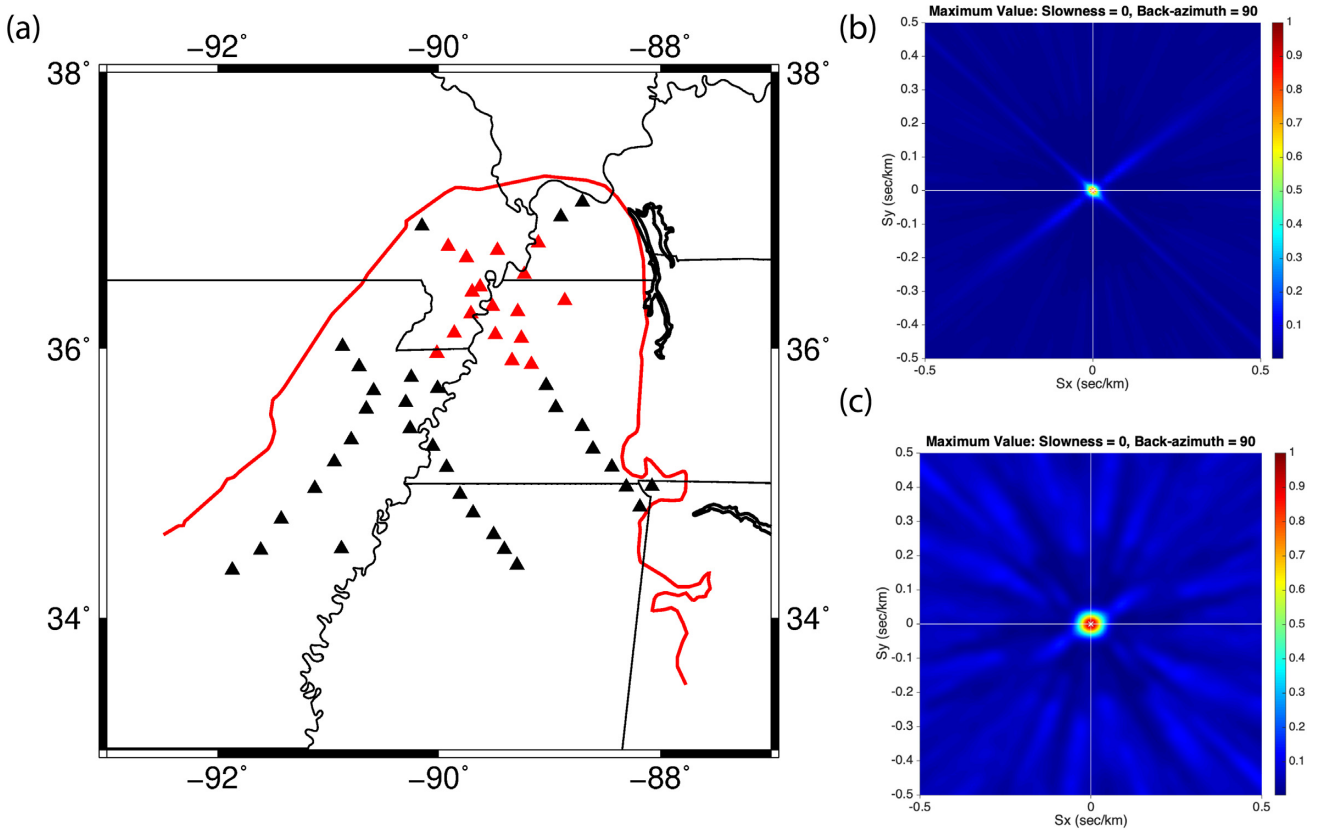

Figure 4. (a) shows the geometry of stations taken to construct two phased arrays to measure azimuth and slowness of observed ambient noise ground motion. Both black and red triangles compose the 50-station array used to analyse primary microseisms in the frequency band of 0.05–0.1 Hz. (b) shows the slowness response of the large array. 17 stations marked with red triangles in (a) are used for 2-D FK analysis of the secondary microseisms in the frequency band 0.1–0.2 Hz. The theoretical array response for this array is shown in (c).

A variety of methods have been used to infer source locations of the ambient noise. Shapiro *et al.* (2006) located sources for 26 s microseisms off the west African coast in the Gulf of Guinea by minimizing the traveltime misfit using a grid search method. Grid searching over the maximum stacked energy (Gu *et al.* 2007; Zeng & Ni 2010) has also been applied to locate sources. Tian & Ritzwoller (2015) and Yang & Ritzwoller (2008) identified different source locations for primary and secondary microseisms by a statistical analysis of the azimuthal distribution of the signal-to-noise ratio (SNR). Behr *et al.* (2013) used three-component plane wave beamforming to infer source locations for primary and secondary microseisms in New Zealand and suggested different backazimuths for primary Rayleigh and Love waves but similar ones for secondary Rayleigh and Love waves.

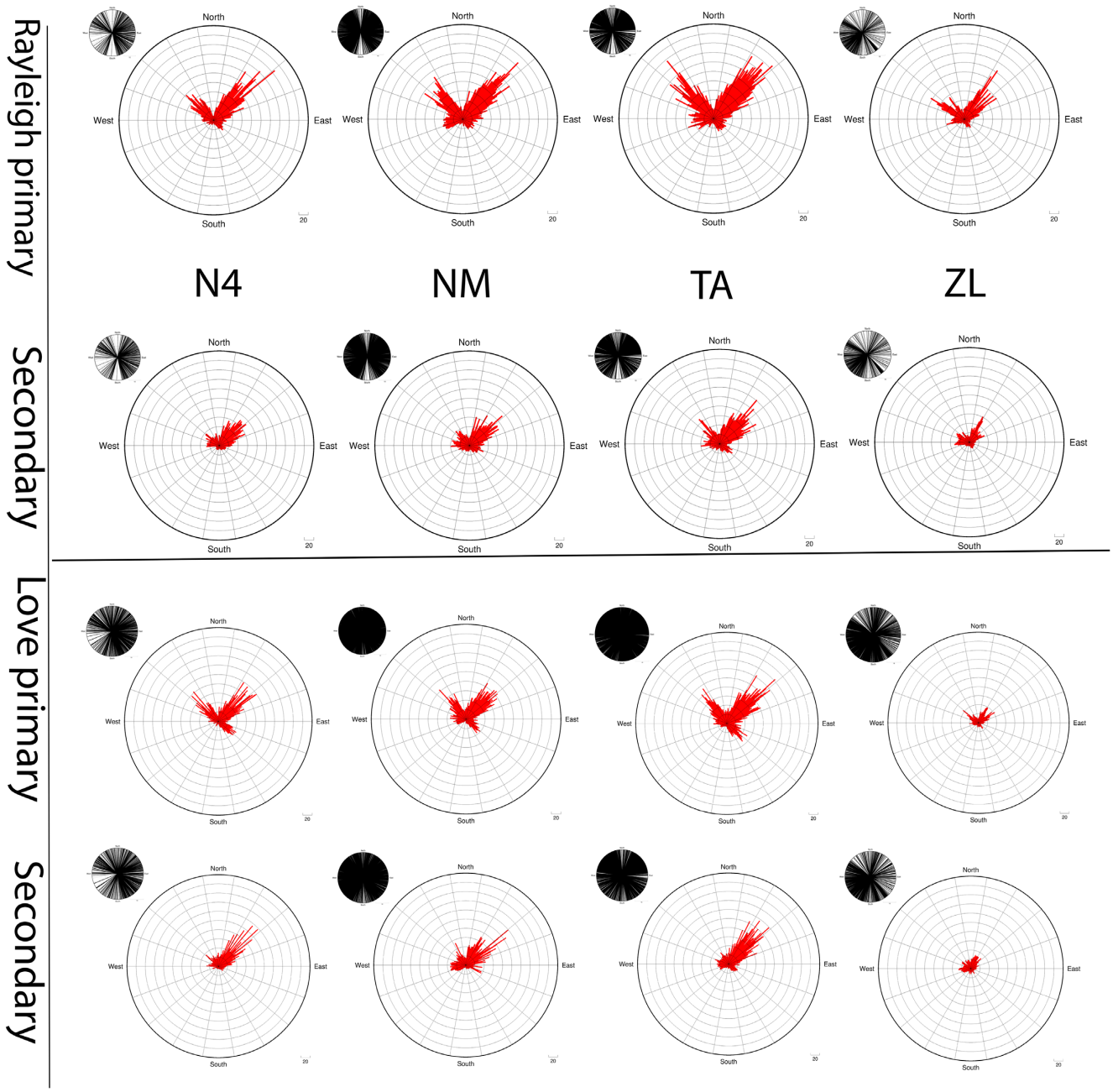

Figure 5. Rose diagrams of SNRs for four networks: N4, NM, TA and ZL. The small rose diagram in the left corner of each plot shows the azimuthal distribution of station pairs. Two, toward-the-source directions (converted from away-from-source directions) can be identified in the northwest and northeast quadrants.

Studies of ambient noise source locations in the Mississippi embayment (ME) are quite limited (Yang & Ritzwoller 2008; Langston *et al.* 2009) but important for the following reasons. The ME is an SSW plunging trough filled with up to 1.5 km of unconsolidated sediments (Fig. 1; Hildenbrand & Hendricks 1995) and hosts one of the most active seismic zones in the North America, the New Madrid seismic zone (NMSZ). Better knowledge of the noise source locations can help to assess the accuracy of previous tomography studies (Liang & Langston 2008, 2009; Chen *et al.* 2016; Liu *et al.* 2018a), which can improve confidence on determining earthquake parameters within the NMSZ. Additionally, the ME sediment variation can also be a potential source for generating sedimentary surface waves (Langston *et al.* 2005, 2009; Liu *et al.* 2018a). Observations of source locations of sedimentary surface waves can help the understanding of the generation mechanisms and how the sediments influence wave propagation.

In this study, we investigate the azimuthal distribution of sources for primary and secondary microseisms, explore the seasonal variation of ambient noise sources by monitoring the changes of the SNRs, amplitude differences and 2-D frequency–wavenumber (FK) power spectra and search for local sources in the embayment using short-period ambient noise ($T < 5$ s).

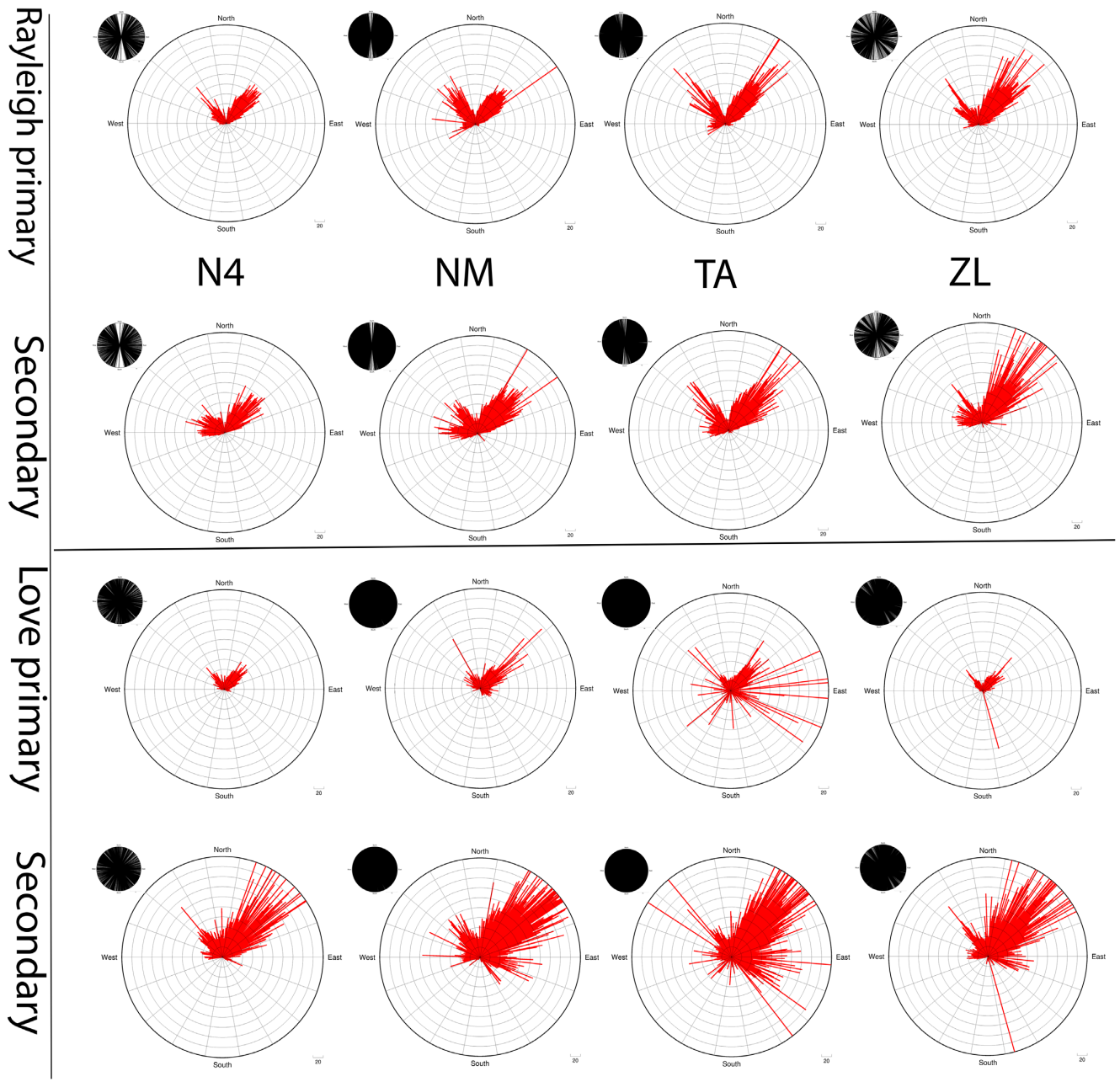

Figure 6. Rose diagrams of amplitude differences for four networks: N4, NM, TA and ZL. Same scheme as Fig. 5. Two major toward-the-source directions, in the northeast and northwest quadrants, can be observed.

2 DATA AND METHODS

2.1 Pre-processing

We use data from 277 broad-band stations (Fig. 1) installed between 1990 and 2018 to compute vertical–vertical (ZZ) and horizontal–horizontal (TT) component CCs. The interstation distances are chosen to be larger than three times the microseism wavelength and data time-series are longer than 30 d in duration. These data have been used to image lithospheric shear wave velocity structure by Liu *et al.* (2018a). We use the MSNoise python package (Lecocq *et al.* 2014) to compute the CCs. The pre-processing procedures can be summarized in the following: (1) broad-band miniseed data are requested from IRIS through the FDSN service; (2) removing the instrument response; (3) bandpassing from 0.05 to 1 Hz; (4) removing transients, earthquake signals and instrumental irregularities using temporal normalization and spectral whitening. Spectral whitening does not change amplitude of surface wave significantly but produces a broader-band signal (fig. 9 in Bensen *et al.* 2007).

We apply statistical analyses of SNRs and positive/negative amplitude differences as well as 2-D FK analysis of the instrument-corrected data to constrain the backazimuths of strong noise sources.

2.2 Signal-to-noise ratio analysis

Energy flux directions for microseisms can be identified from the azimuthal distribution of SNRs (Yang & Ritzwoller 2008; Tian & Ritzwoller 2015). The SNR is defined to be the ratio between the maximum absolute amplitude of crustal surface wave arrivals

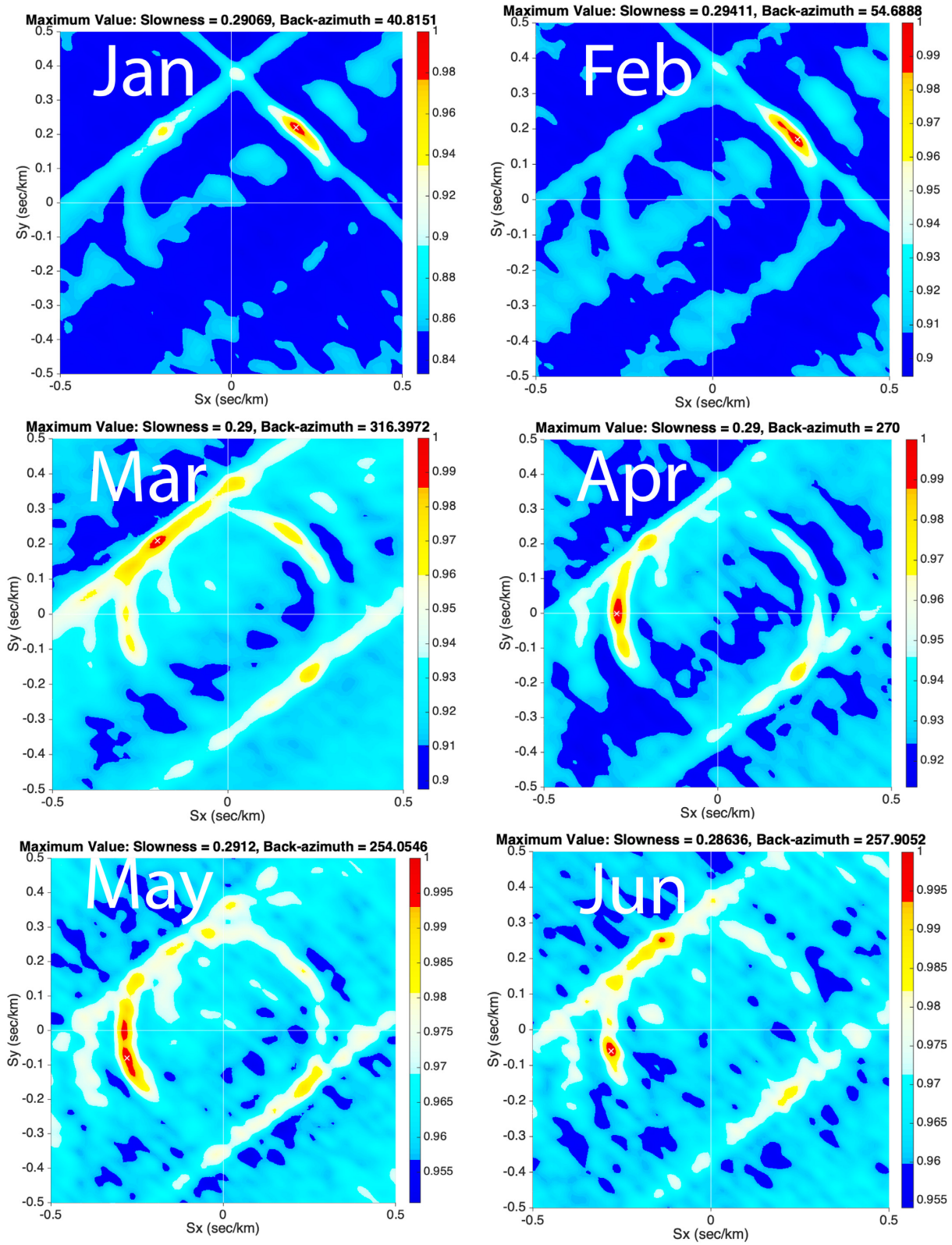

Figure 7. Monthly power spectra for Rayleigh primary microseisms in 2014. Energy flux with backazimuths of ∼ 40° and ∼ 320° emerge during the whole year but the energy is stronger in winter than summer. Energy flux with backazimuths of ∼ 120° and ∼ 260° become visible from March to September.

(∼3 km s^{-1}) and the root-mean-squared (RMS) amplitude of noise in the coda window. In the primary (10–20 s) or secondary (5–10 s) microseism passband, we define the coda window as the last 200 s of CCs, where no direct surface wave arrivals are observed (Fig. 2). Yang & Ritzwoller (2008) suggested that the RMS amplitude of noise after the major crustal surface wave arrival is similar for the CCs within the same seismic array (Supporting Information Fig. S1). Fig. 3(a) shows CCs between the virtual source at HENM

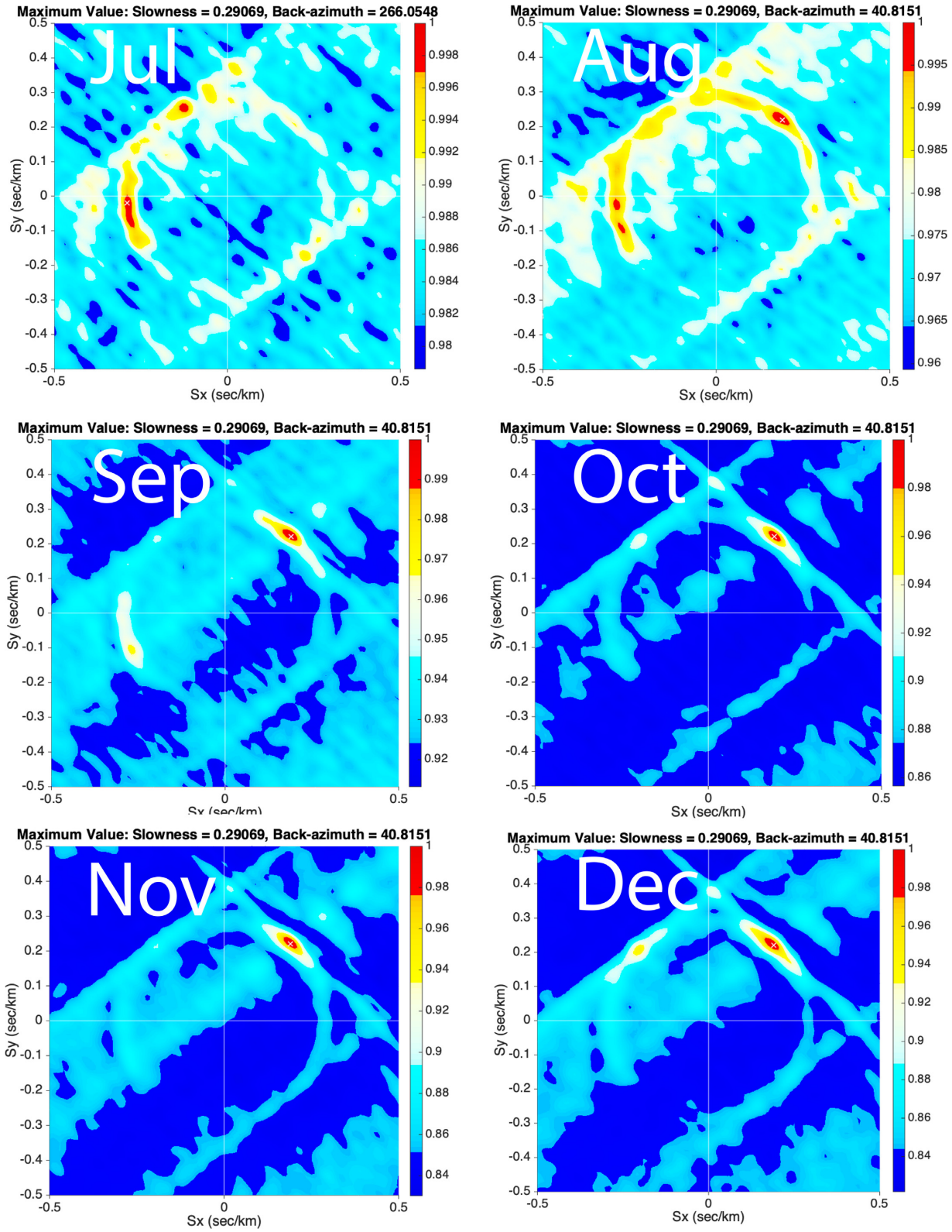

Figure 7. (*Continued.*)

station and all surrounding stations. The positive lag portion of the CCs is the outgoing wave from the virtual source. For a CC between the virtual source A and station B, the outgoing wave from the station A is the incoming wave for the station B. Thus, we only use positive lags of CCs to compute the SNR. We then correct SNR measurements for geometric spreading (normalizing to an interstation distance of 300 km) through $\mathrm{SNR}_{\mathrm{corrected}} = \mathrm{SNR} * \sqrt{D/300}$, where D is the interstation distance in km. A simplified assumption from Tian & Ritzwoller (2015) indicates that SNR increases as the square root of number of days to be stacked. We then

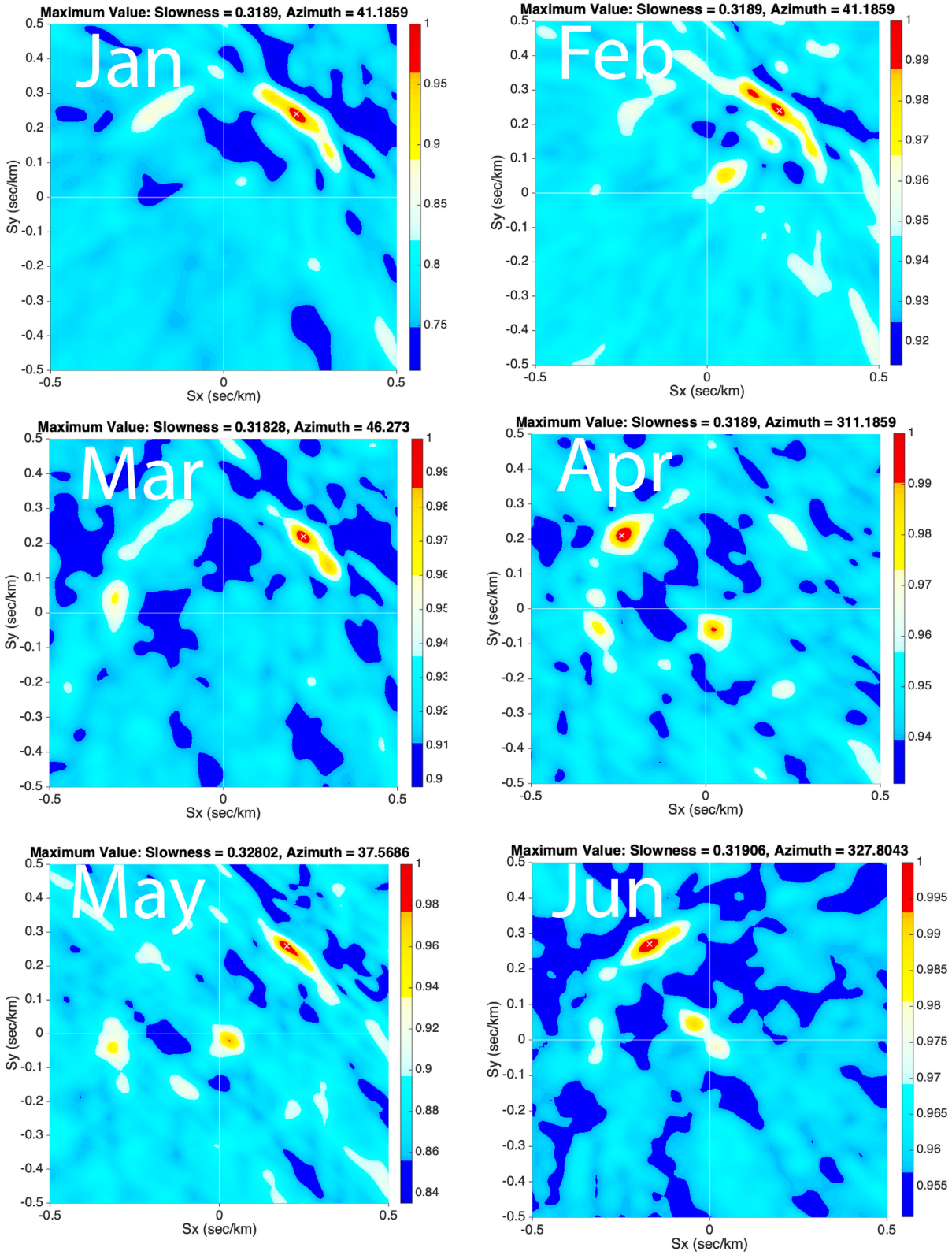

Figure 8. Monthly power spectra for Rayleigh secondary in 2014. Two strong energy fluxes with the backazimuths of ∼ 40° and ∼ 320° emerge in northeast and northwest quadrants for the whole year. Two additional energy fluxes emerge in the southeast and southwest quadrants from April to July.

correct SNR measurements (normalizing to 30 d stack) through $\mathrm{SNR}_{\mathrm{final}} = \mathrm{SNR}_{\mathrm{corrected}} * \sqrt{30/N}$, where N is number of days to be stacked. All final corrected SNR measurements for all CCs related to the virtual source A, with different azimuths, are used to construct a rose diagram (Fig. 3b). The azimuths (Fig. 3c) here are from the virtual source A to surrounding stations. The bars point to the wave propagation direction for sources of microseisms (away-from-the-source). If noise sources are distributed homogeneously

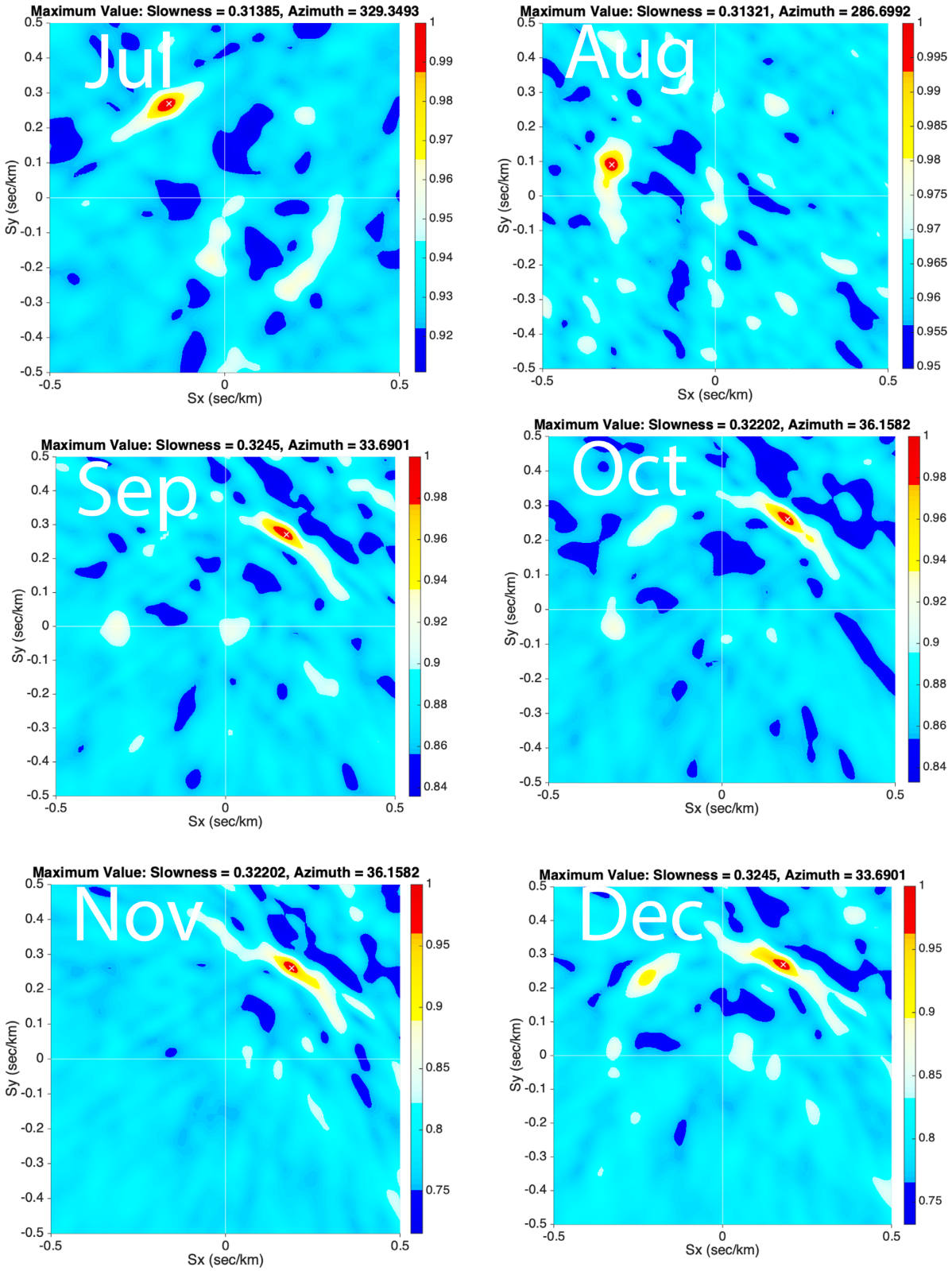

Figure 8. (*Continued.*)

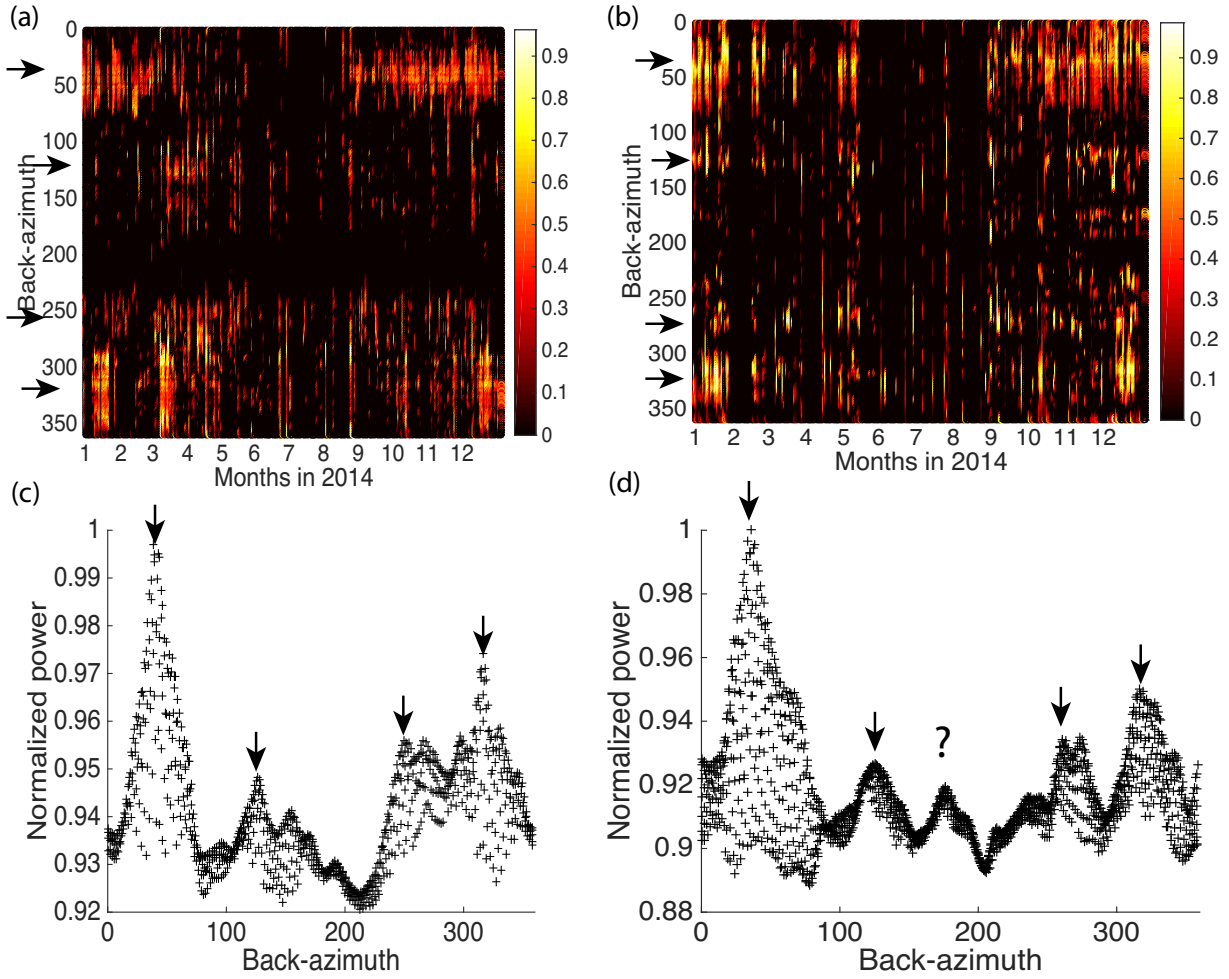

Figure 9. Seasonal variations of power spectra for primary (a and c) and secondary (b and d) microseisms with backazimuth. We first remove the average of the power spectra. Power spectra with the slowness between 0.27 and 0.35 s km^{-1} are binned based on the backazimuths, from 0° to 360° with 2° interval. In each bin, we use the maximum to represent the power. We stack power spectra of each day and use the maximum to normalize the power. Four major backazimuths, ∼ 50°, ∼ 125°, ∼ 260° and ∼ 320°, can be identified. A slight difference, ∼ 255° for Rayleigh primary and ∼ 270° for Rayleigh secondary, might indicate different source locations.

in azimuth, then each SNR value should have the same length. If there is a dominant source direction, then bars will get relatively longer in the direction away-from-the-source.

2.3 Amplitude-difference analysis

We also propose to use the amplitude difference of crustal surface waves seen at positive and negative lags of the CCs to estimate the strength of signal. The amplitude difference is defined as $\mathrm{Amp}_{\mathrm{diff}} = (\mathrm{Amp}_{\mathrm{pos}} - \mathrm{Amp}_{\mathrm{neg}}) * 10\,000$, where $\mathrm{Amp}_{\mathrm{pos}}$ and $\mathrm{Amp}_{\mathrm{neg}}$ are the maximum amplitudes of crustal surface waves at positive and negative lags of the CCs, respectively. The amplitude difference is exaggerated 10 000 times for better comparison with the SNR measurements. The amplitude difference is also corrected for the geometric spreading and the number of days as outlined in the previous section. If the corrected amplitude difference is larger than 200, we set the value to be 200. For a CC between the virtual source A and the receiver B, if the amplitude of the crustal surface wave on the positive lag is larger than that on the negative lag, the backazimuth from receiver B (Fig. 3c) indicates the direction of the source. Otherwise, we use azimuth. A collection of amplitude differences for all CCs related to the virtual source A is used to construct a rose diagram indicating the source directions (toward-the-source).

Compared to the SNR analysis, the amplitude-difference measurement does not depend on the RMS amplitude of random noise, if the Green's function signal is significantly higher amplitude than the noise. It may be more suitable for regions where the random component of the noise field remaining after correlation varies temporally and spatially. If two microseisms with the same amplitude propagate across the array in opposite directions over the time length of the correlation, the amplitude difference will be zero, that is, the positive and negative lag Green's functions will be of equal amplitude. However, if microseism sources in one direction are higher amplitude than in the opposite direction, the Green's function from the station towards the high-amplitude direction will be larger. It is a different way to represent the same information in the SNR analysis and uses the same assumptions in that a direction is implied by the strength of the Green's function. Obviously, the measurement will be limited by

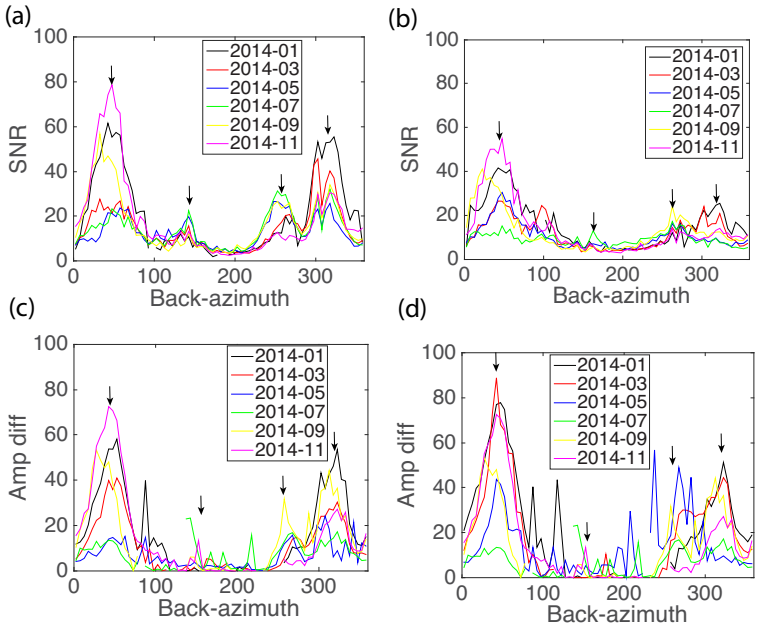

Figure 10. Seasonal variations of monthly average SNRs and amplitude differences for Rayleigh primary (a and c) and secondary (b and d) microseisms. Four major backazimuths, 40°, 140°, 260° and 320°, are observed in the azimuthal distribution of primary and secondary microseisms. A small difference, ∼ 255° for Rayleigh primary and ∼ 270° for Rayleigh secondary, can also be observed. For noise with backazimuths of ∼ 140° and ∼ 260°, average SNRs and amplitude differences from May to September are higher than those from November to March. For noise with backazimuths of ∼ 40° and ∼ 320°, average SNRs and amplitude differences from September to March are higher than those from May to July.

the SNR of the weakest half of the correlation seismogram which is why we apply a threshold of 200 in the difference. It is a technique to represent the amplitude differences in CCs in a simple, intuitive way.

2.4 2-D frequency–wavenumber analysis

We verify the source directions determined from the azimuthal distribution of SNRs and amplitude differences through direct 2-D FK analysis of displacement seismograms containing microseisms for a subset of stations used as a phased array (Capon 1973; Aki & Richards 2002; Langston *et al.* 2009; Behr *et al.* 2013). The reference station in the 2-D FK analysis for primary microseisms is the centre of an array composed of 50 stations deployed in 2014 as part of the Northern Embayment Lithosphere Experiment (Fig. 4). The location of the centre is defined by averaging latitude and longitude of array station locations. In addition, we construct a more compact array from 17 stations in the northern embayment to analyse the secondary microseisms. We use a broad-band frequency–wavenumber technique where *f*–*k* spectra are averaged over a narrow frequency band (Nawab *et al.* 1985). Primary microseisms were analysed in the 0.05–0.1 Hz band and secondary microseisms were analysed in the 0.1–0.2 Hz band.

We compute monthly 2-D FK power spectra to investigate seasonal variations in microseism wave direction and slowness. This is done by cutting the time-series into 24 hourly segments, computing 2-D FK power spectra for each 1-hr segment, and then stacking hourly 2-D power spectra into monthly power spectra. In attempt to obtain better temporal resolution, we also compute the 2-D FK power for each day.

3 RESULTS

3.1 Azimuthal changes in SNRs and amplitude differences

Investigating seasonal variations of SNRs and amplitude differences can help reveal backazimuths of noise sources. The hypothesis that microseisms originate from arrivals of strong storms has been confirmed by Stehly *et al.* (2006). Strong storms appear in the northern Pacific and Atlantic during Northern Hemisphere winter and the southern Indian and Pacific Oceans during Northern Hemisphere summer (Young 1999; Stehly *et al.* 2006). We use the vertical component of 84 broad-band stations (Fig. 1) with continuous recording to compute the CCs over the months of 2014. For each month, SNRs and amplitude differences are computed from all CCs. Because the directional output from SNRs and amplitude differences are different, away-from-the-source in SNR and toward-the-source for amplitude difference, we convert away-from-the-source to toward-the-source for better comparison. We then bin SNRs and amplitude differences into 5° backazimuth intervals. The RMS of SNRs and amplitude differences are computed. Collections of azimuthal variations of SNRs or amplitude differences in different seasons can provide direct observations of major source backazimuths.

In the following, ‘Rayleigh primary’ and ‘Rayleigh secondary’ correspond to the ZZ correlation Green’s functions for primary and secondary microseisms, respectively. Likewise, ‘Love primary’ and ‘Love secondary’ correspond to the same microseisms for the TT correlation Green’s functions. We compute 13 445 and 11 977 ZZ and TT component CCs, respectively. For each CC, we compute the SNR and amplitude difference. We compare the azimuthal distribution of station pairs with SNRs and amplitude differences computed from four networks: Central and Eastern US National network (N4),

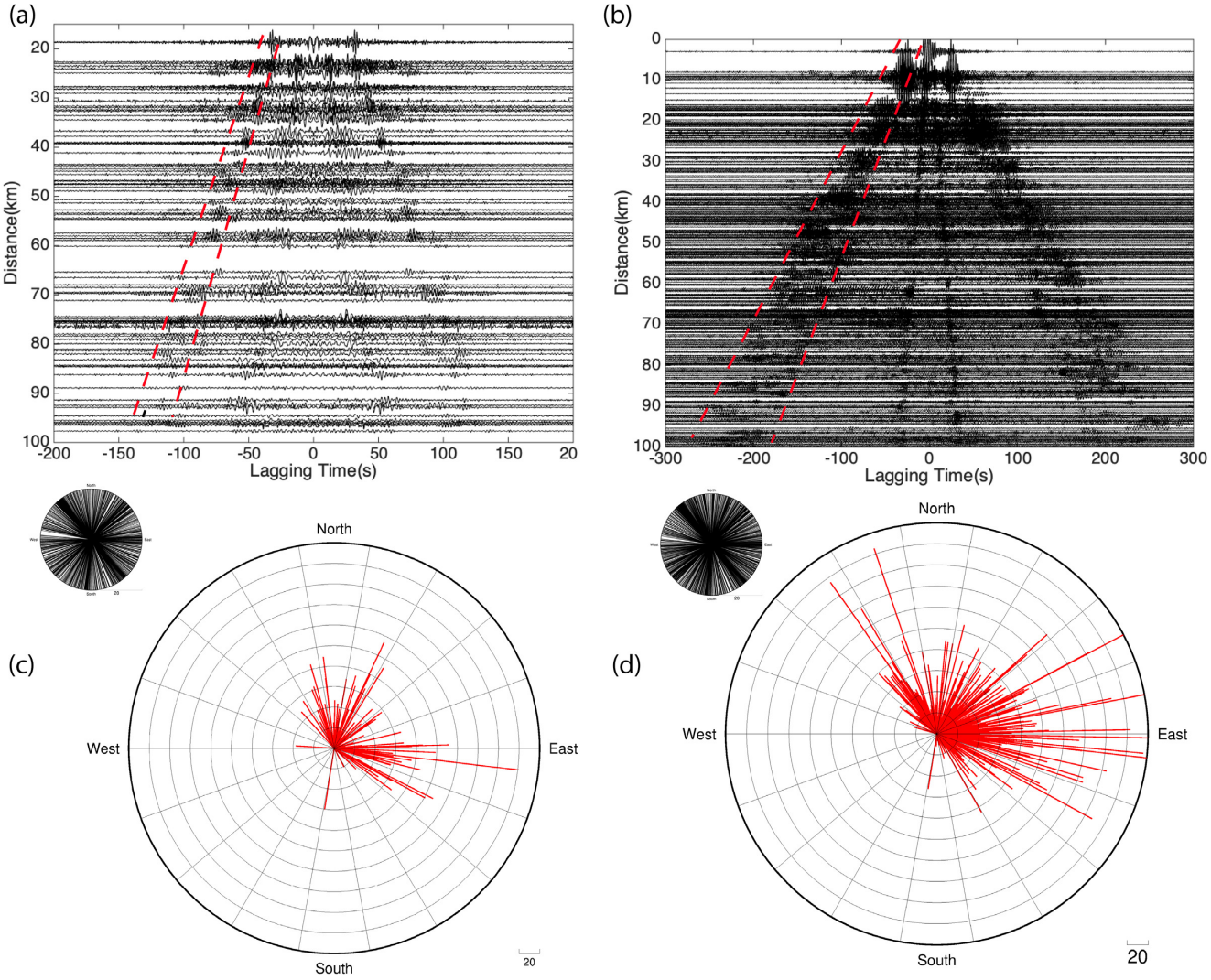

Figure 11. Directionality of sedimentary Rayleigh and Love waves. (a) ZZ component cross-correlations showing arrivals of sedimentary Rayleigh waves ($\sim$0.75 km s^{-1}) within 100 km interstation distance. Sedimentary surface wave arrivals are marked between two dashed lines. (b) Arrivals of sedimentary Love waves ($\sim$0.45 km s^{-1}). (c) Azimuthal distribution of amplitude differences of sedimentary Rayleigh waves. (d) Azimuthal distribution of amplitude differences of sedimentary Love waves. Weak energy arrivals are observed in the third quadrant of the rose diagram. Weak energy arrivals correlate to the direction of widening of the ME basin.

Cooperative New Madrid Seismic network (NM), USArray Transportable Array (TA) and Northern Embayment Lithospheric Experiment (ZL). Station pair azimuthal coverage is excellent for each network (Figs 5 and 6). Two major toward-the-source directions can be identified in the azimuthal distribution of SNRs (Fig. 5) and amplitude differences (Fig. 6). We observe no significant differences between Rayleigh (or Love) primary and secondary microseisms.

3.2 Changes in wavenumber spectra

Slowness and backazimuth determinations require that signals correlate across our large regional arrays (Fig. 4). The stacked monthly power spectra for Rayleigh primary microseisms are shown in Fig. 7. Much of the ambient noise field is seen to be roughly homogeneous since there is a clear circular ring of power with a slowness of approximately 0.29 s km^{-1}. However, there are also clear maxima on the ring indicating that seismic waves do have dominant directions. Energy flux with backazimuths of $\sim 40^\circ$ and $\sim 320^\circ$ emerge for the whole year but the energy is stronger in winter than summer. Energy flux with backazimuths of $\sim 120^\circ$ and $\sim 260^\circ$ becomes visible from March to September. Sources of secondary microseisms are distinctly heterogeneous (Fig. 8). Major energy flux emerges in northeast and northwest quadrants. Weak energy flux can be observed in southwest and southeast quadrants in April, May and June. We investigate how the daily power spectra change with backazimuth (Figs 9a and b). We first set up a threshold:

$$P\left(S_x,\ S_y\right) = \begin{cases} P\left(S_x,\ S_y\right) & \text{if } P\left(S_x,\ S_y\right) > 1.05\bar{P} \\ 0 & \text{otherwise} \end{cases},$$

where P is power with slowness of S_x and S_y in x and y directions, respectively. $\bar{P}$ is the RMS value of daily power spectra with different slowness values in x and y directions. 1.05 is selected to best show major power in the spectra. We then pass the daily

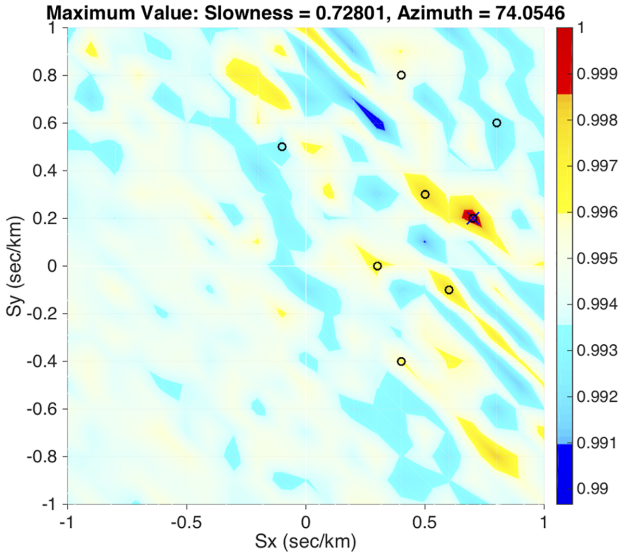

Figure 12. Yearly power spectra for the sedimentary Rayleigh wave in the passband of 0.2–1 Hz. We use the same secondary microseism array (red triangles of Fig. 4). Blue cross marks the strongest energy arrivals in 2014 with azimuth of $\sim 74^\circ$ and slowness of 0.73 s km^{-1}. Black circles mark monthly strong arrivals. Power spectra for each month is shown in Supporting Information Fig. S4. We do not observe strong energy arriving from the third quadrant (southwestern direction).

power spectra through the defined threshold and bin the sampled power spectra with slowness from 0.27 to 0.35 s km^{-1} and a 2° azimuth interval and use the average value in each bin to represent the power. Applying threshold on the daily power spectra can help to better observe power difference across different azimuths for different days. To estimate the exact azimuths of energy flux from 2-D FK power spectra, we investigate how the yearly power spectra change with backazimuth (Figs 9c and d). This is done by stacking power spectra for a whole year and then normalizing the stack by the maximum power attained in the stack. We then examine the sampled power in the normalized stack within the slowness ring of 0.27 to 0.35 s km^{-1} by plotting each sampled *fk* power value versus azimuth where slowness in both East and North is sampled by 0.01 s km^{-1}. Four major backazimuths can be identified. We observe a small difference, $\sim 255^\circ$ for Rayleigh primary and $\sim 270^\circ$ for Rayleigh secondary, on the backazimuths of noise energy flux in the southwest quadrant.

3.3 Seasonal variability of SNRs and amplitude differences

We also compute 1670 vertical component CCs to investigate seasonal variations of azimuthal distribution of SNRs and amplitude differences. In Fig. 10, different coloured lines represent average SNRs and amplitude differences for different months in 2014. Four major backazimuths, $\sim 40^\circ$, $\sim 140^\circ$, $\sim 260^\circ$ and $\sim 320^\circ$, are identified in the azimuthal distribution of the SNRs and amplitude differences. A small difference, $\sim 255^\circ$ for Rayleigh primary and $\sim 270^\circ$ for Rayleigh secondary, can also be observed. For ambient noise Green's functions with backazimuths of $\sim 140^\circ$ and $\sim 260^\circ$, average SNRs and amplitude differences from July to September are higher than those from November to March. For Green's functions with backazimuths of $\sim 40^\circ$ and $\sim 320^\circ$, average SNRs and amplitude differences from November to March are higher than those from May to July.

3.4 Directionality of the sediment surface wave

We compute 1247 and 989 pairs of TT and ZZ component CCs, respectively, for station pairs with interstation distance less than 100 km (Supporting Information Fig. S2). We observe 390 pairs of CCs with low-velocity sedimentary Love waves (group velocity of $\sim$450 m s^{-1}) and 86 pairs of Rayleigh waves (group velocity of $\sim$750 m s^{-1}; Fig. 11 and Supporting Information Fig. S3). Station pairs displaying coherent low-velocity sedimentary surface wave arrivals in the passband of 0.2–1 Hz (Supporting Information Fig. S3) are all inside the ME (Supporting Information Fig. S2). Rose diagrams of amplitude differences for sedimentary Rayleigh and Love waves show that arrivals from the third quadrant (southwestern direction) are relatively weak compared to NW, NE and SE quadrants (Figs 11c and d). Frequency–wavenumber analysis (Supporting Information Fig. S4 and Fig.12) of ambient noise data for the entire year recorded by the smaller array (Fig. 4) show that discrete noise sources in the NE quadrant dominate the response and that wave energy from the SW is generally subdued. The strongest energy is arriving from the northeast with a backazimuth of $\sim 74^\circ$ and slowness of ~ 0.7 s km^{-1}. Monthly power spectra show that the slowness of sedimentary surface wave ranges from 0.5 to 1 s km^{-1} (Fig. 12 and Supporting Information Fig. S4).

4 DISCUSSION

4.1 Source locations for primary and secondary microseisms

A simple backprojection along the great circle from the network location can provide an idea of source locations. The backprojection needs two major parameters, the location of the array and the backprojection directions. We fit four joint Gaussian functions to the azimuthal distribution of SNRs to estimate the means and standard deviations of backazimuth because we observe four SNR peaks in it (Fig. 13). We use the centre of array (90° W, 35° N) as our reference location with the means plus and minus 1 standard deviation as our backprojection directions. We use a nonlinear regression fitting function of Matlab, fitnlm (Holland & Welsch 1977; DuMouchel & O'Brien 1989; Seber & Wild 2003), to compute the means and standard deviations. The fitting function has the form of: $y = a + c_1 * e^{-(x-c_2)^2}/c_3 + d_1 * e^{-(x-d_2)^2}/d_3 + m_1 * e^{-(x-m_2)^2}/m_3 + n_1 * e^{-(x-n_2)^2}/n_3$, in which a, c_1, c_2, c_3, d_1, d_2, d_3, m_1, m_2, m_3, n_1, n_2 and n_3 are unknown.

Backprojection directions measured from the different methods are similar to each other for primary and secondary microseisms (Table 1). A simple backprojection (Fig. 14) using the Gaussian mean and standard deviation provides insight on the source locations but cannot constrain the exact locations because distance from the array is not known. The exact locations of noise sources can be determined from triangulation of backprojections from at least two independent arrays.

Noise sources for backazimuths of $\sim 45^\circ$ and $\sim 320^\circ$ are stronger than those from the backazimuths of $\sim 125^\circ$ and $\sim 260^\circ$. The amplitude of ambient noise waves may be related to the distance to the noise source, the amplitude of noise source, or azimuthal variations in anelastic attenuation.

Noise sources with the backazimuth of $\sim 45^\circ$ have the strongest energy. Backprojection from the centre of the network shows that the source locations for primary and secondary microseisms are in the northern Atlantic Ocean or along North American coasts. The strongest energy source in the northern hemisphere occurs during

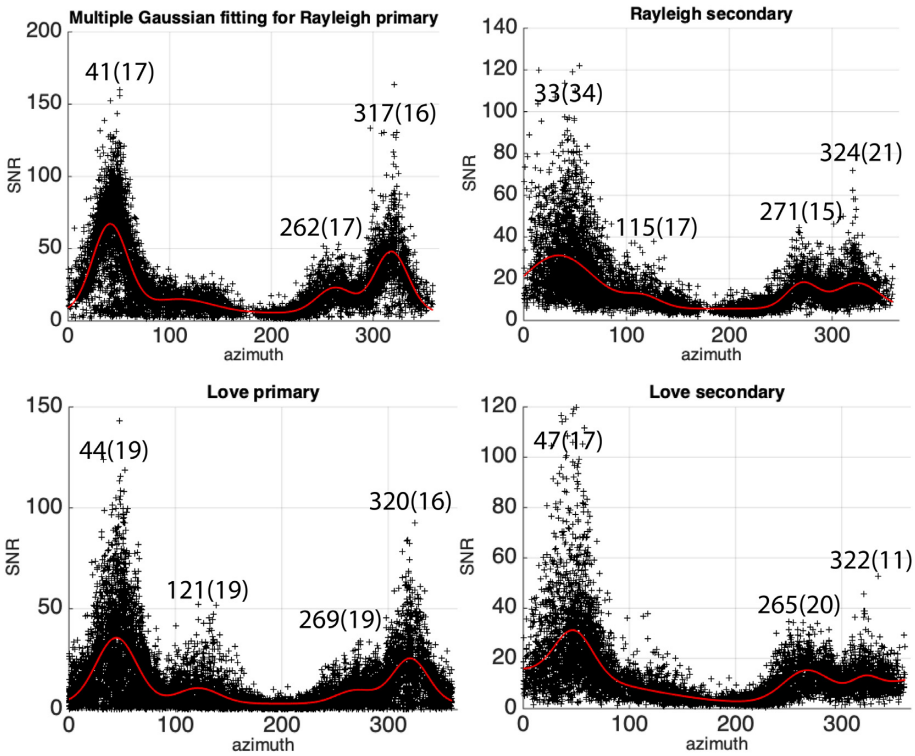

Figure 13. Multiple Gaussian function fitting to obtain the azimuthal distribution of SNR measurements. Values over local peaks of fitting curves are the Gaussian means and standard deviations (in parentheses).

Table 1. Comparison of backazimuths from different methods.

Methods	Backazimuth1	Backazimuth2	Backazimuth3	Backazimuth4
Gaussian fitting of SNRs (Fig. 13, Rayleigh primary)	41° ± 17°	N/A	262° ± 17°	317° ± 16°
Gaussian fitting of SNRs (Fig. 13, Rayleigh secondary)	33° ± 34°	115° ± 17°	271° ± 15°	324° ± 21°
Gaussian fitting of SNRs (Fig. 13, Love primary)	44° ± 19°	121° ± 19°	269° ± 19°	320° ± 16°
Gaussian fitting of SNRs (Fig. 13, Love secondary)	47° ± 17°	N/A	265° ± 20°	322° ± 11°
Seasonal variations of SNR and amplitude difference (Fig. 10, Rayleigh primary)	∼ 40°	∼ 140°	∼ 260°	∼ 320°
Seasonal variations of SNR and amplitude difference (Fig. 10, Rayleigh secondary)	∼ 40°	∼ 150°	∼ 270°	∼ 320°
2-D FK power spectra (Fig. 9, Rayleigh primary)	∼ 45°	∼ 125°	∼ 255°	∼ 320°
2-D FK power spectra (Fig. 9, Rayleigh secondary)	∼ 45°	∼ 125°	∼ 270°	∼ 320°

winter and appears in the Atlantic Ocean (Stehly *et al.* 2006; Ardhuin *et al.* 2011). Kedar *et al.* (2008) suggested that sources of secondary microseisms for this strong energy are in the deep water south of Greenland. Retailleau *et al.* (2017) proposed that sources for primary microseisms are along the coast of Greenland. Similar source locations for body waves at 0.1–0.3 Hz have also been observed through beamforming analysis by Landès *et al.* (2010). Langston *et al.* (2009), suggested that source locations for microseisms in the 4–5 s period passband can be along the coast of Newfoundland in northeastern North America based on wave gradiometry and frequency–wavenumber analysis. A wide-angle triangulation (Cessaro 1994) also suggested the sources for primary microseisms are along the coasts of Newfoundland. Since previous studies (Cessaro 1994; Bromirski & Duennebier 2002) infer shallow sources for primary microseisms, we suggest that sources for Rayleigh and Love primary microseisms are near the coasts of Newfoundland or Greenland. The source of secondary microseisms can be off the coast of Newfoundland and be related to the interaction between ocean swell with coastal reflections or in the deep water south of Greenland.

For ambient noise with a backazimuth of ∼ 125°, noise energy flux is stronger in summer than in winter suggesting that sources are in the Southern Hemisphere. Backprojections along the great circle arc suggest a location near the Atlantic coast of South America. The source for secondary microseisms can also be near the South American coast or in the southern Atlantic Ocean.

In the backazimuth range of ∼ 260°, previous workers have proposed that the sources might be in the southern Pacific Ocean and near the coastal region of Australia or New Zealand. Tian & Ritzwoller (2015) suggested that the sources for primary microseisms with the backazimuth of ∼220° can be in the Pacific Ocean of the Southern Hemisphere. Stehly *et al.* (2006) also observed that sources for Rayleigh primary microseisms can be generated in the southern Pacific Ocean and near the southern and eastern coastal regions of Australia and New Zealand as well as the southern Indian Ocean during the Northern Hemisphere summer. Gerstoft *et al.*

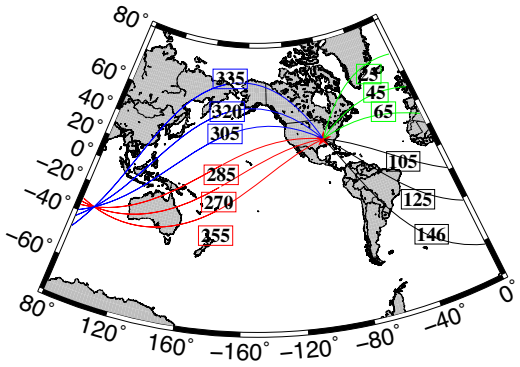

Figure 14. Great circle backprojections from the Central U.S. For energy flux from the backazimuth of 45°, noise sources can be along the coast of Newfoundland or Greenland for primary microseisms and in the deep water of south of Greenland for secondary microseisms. Noise sources are along the coasts of South America for primary microseisms with the backazimuth of 125° but also in the southern Atlantic Ocean for secondary microseisms. For primary microseisms with the backazimuth of 255°, noise sources can occur along the coasts of Australia or New Zealand. For secondary microseisms with the backazimuth of 270°, sources are in the southern Pacific Ocean. Noise sources for primary microseisms with the backazimuth of 320° can occur along the coasts of Alaska and Canada. Secondary microseisms can originate along the coasts being related to coastal reflections or they may occur in the deep Pacific Ocean.

(2008) and Landès *et al.* (2010) observed possible source locations for 0.1–0.3 Hz body waves in the southern Pacific. A slight difference on propagation directions (∼255° for Rayleigh primary and ∼270° for Rayleigh secondary in Figs 9 and 10) may indicate that sources are in different regions. Primary microseisms (∼255°) can be generated near the southern coast of Australia or northwest coast of New Zealand (Stehly *et al.* 2006; Reading *et al.* 2014). Great circle backprojections indicate that secondary microseisms (∼270°) can be in the deep Pacific Ocean of the Southern Hemisphere.

Many studies have indicated that ambient noise in the backazimuth range of ∼ 320° could be generated near the coasts of Canada and Alaska or in the deep northern Pacific Ocean. Tian & Ritzwoller (2015) proposed that primary microseisms identified in the Juan de Fuca plate area are generated in shallow water near the Graham island. Stehly *et al.* (2006) suggested that primary microseisms might be generated from two low energy sources, one near the coast of Alaska and the other close to Japan. Gerstoft *et al.* (2008) and Landès *et al.* (2010) proposed sources for seismic body waves that could be in the deep ocean of the Pacific. Ardhuin *et al.* (2011) suggested that coastal reflections can significantly increase the secondary microseisms along the western coast of Alaska and California. Primary microseisms can be generated near the coastlines of Alaska and Canada. Secondary microseisms can also originate near coasts and be related to coastal wave reflections or, alternatively, have a source in the deep Pacific.

4.2 Directionality of the sedimentary surface wave

Sedimentary surface waves can be used to image the sediment velocity structure and understand wave propagation properties (Langston *et al.* 2009; Lin *et al.* 2013). The dominant frequency range for the sedimentary surface wave in the ME is 0.2–1 Hz (Supporting Information Fig. S3), which is similar to Langston *et al.* (2005, 2009). Langston *et al.* (2005) observed sedimentary surface waves in the passband of 0.4–1.5 Hz from an explosion experiment. Langston *et al.* (2009) also observed that a slow, roughly 1 km s^{-1}, sedimentary surface wave emerged in the passband of 3–5 s within the ME through frequency–wavenumber analysis of ambient noise suggesting a local noise source. Observed strong reverberations for station HBAR inside the ME over the frequency range of 0.2–3 Hz and suggested that the mechanism was due to conversion of *S* waves to surface waves near the edges of the basin. We observe that the strongest energy arrives from northeastern directions with a phase velocity of only 1.4 km s^{-1} (Fig. 12). Weak energy arrivals from 100° to 220° (Figs 11 and 12) correlates with the direction in which the basin widens. A possible explanation is that thick sediments in the southern ME attenuate more energy than thinner sediments in the northern ME. In Supporting Information Fig. S2, low-velocity surface waves can only be observed for station pairs inside the ME implying that they are trapped sedimentary surface waves from local sources. Trapped surface waves have been observed at Kobe, Japan (Kawase 1996; Hallier *et al.* 2008), Tokachi basin (Furumura & Sasatani 1996), Oasaka basin (Hatayama *et al.* 1995), Grenoble basin (Cornou *et al.* 2003) and Los Angeles basin (Husker *et al.* 2006). They are likely caused by conversion from an incident crustal surface wave or an *S* wave at the edge of the basin (Hatayama *et al.* 1995; Field 1996; Furumura & Sasatani 1996; Kawase 1996; Nayaran 2012). We note this interesting observation in our ambient noise data set. Investigation of the nature of this local ambient noise source will likely need relatively long term array deployments to more precisely locate source areas and to investigate the basin velocity structure in detail.

5 CONCLUSIONS

We investigate source locations of Rayleigh and Love primary/secondary microseisms through statistical analyses of SNRs and amplitude differences of empirical CC Green's functions and 2-D FK analysis of ambient noise ground motions. We use 277 broad-band stations to construct 13 445 and 11 977 ZZ and TT component CCs. Two major directions can be identified in the azimuthal distribution of SNRs and amplitude differences for primary and secondary microseisms. We also use 84 stations which continuously record in 2014 to estimate seasonal variations of seismic noise. Seasonal variations of SNRs and amplitude differences locate another two weak noise sources in the Southern Hemisphere. Additionally, we use 390 TT and 86 ZZ component CCs to investigate generation mechanisms of sedimentary surface waves. Because low-velocity sedimentary surface waves can only be observed inside the ME, they are trapped surface waves from local sources. Weak energy arrivals from the south and southwest might be related to the widening direction of the basin where anelastic attenuation may be greater due to thicker sediments. Further experimental and theoretical work is needed to better understand the generation mechanisms of the sedimentary surface waves.

Four major backazimuths, ∼ 45°, ∼ 125°, ∼ 255° and ∼ 320°, are identified in the primary microseism band. For ambient noise with a backazimuth of ∼ 255°, noise energy flux is stronger in Northern Hemisphere summer than in winter indicating that noise sources must be in the Southern Hemisphere. A simple backprojection reveals that noise sources can be along the coast of Australia or New Zealand. For ambient noise with a backazimuth of ∼ 320°, major sources could be along the coasts of Canada and Alaska, consistent with regions identified by Tian & Ritzwoller (2015) and Stehly *et al.* (2006). For noise with the backazimuth of ∼ 45°, sources can be near the coasts of Newfoundland and/or Greenland.

For ambient noise with a backazimuth of ∼ 125°, strong energy flux in Northern Hemisphere summer suggests that noise sources are in the Southern Hemisphere. A simple backprojection reveals that sources can be along the southeast Atlantic coast of South America.

In the secondary microseism band, four major azimuths, ∼ 45°, ∼ 125°, ∼ 270° and ∼ 320°, are observed. Sources for noise with the backazimuth of ∼ 270° can be in the Southern Hemisphere Pacific Ocean, where sources for body waves were suggested by Gerstoft *et al.* (2008) and Landeés *et al.* (2010). Sources for noise with backazimuth ∼ 320° can be near the coasts of Alaska and Canada or in the deep Pacific Ocean (Gerstoft *et al.* 2008; Landeés *et al.* 2010). Sources for noise with backazimuth ∼ 40° can be near the coasts of Newfoundland and Greenland or in the deep ocean south of Greenland.

ACKNOWLEDGEMENTS

The authors appreciate critical and constructive reviews from two anonymous reviewers, which helped to improve this paper. We appreciate financial support from Center for Earthquake Research and Information (CERI), University of Memphis. The authors are grateful to Thomas Lecocq who developed the open-access code, MSNoise (www.msnoise.org), to compute CCs. All microseism noise data can be obtained from the IRIS (www.iris.edu) Data Management Center through FDSN service.

REFERENCES

Amante, C. & Eakins, B.W., 2009. ETOPO1 arc-minute global relief model: procedures, data sources and analysis, U.S. Department of Commerce, National Oceanic and Atmospheric Administration, National Environmental Satellite, Data, and Information Service, National Geophysical Data Center, Marine Geology and Geophysics Division, Boulder, CO, http://purl.access.gpo.gov/GPO/gpo441.

Ardhuin, F., Stutzmann, E., Schimmel, M. & Mangeney, A., 2011. Ocean wave sources of seismic noise, *J. geophys. Res.,* **116**(C9), doi:10.1029/2011JC006952.

Aki, K. & Richards, P.G., 2002. *Quantitative Seismology,* University Science Books.

Behr, Y., Townend, J., Bowen, M., Carter, L., Gorman, R., Brooks, L. & Bannister, S., 2013. Source directionality of ambient seismic noise inferred from three-component beamforming, *J. geophys. Res.,* **118**(1), 240–248.

Bensen, G., Ritzwoller, M., Barmin, M., Levshin, A., Lin, F., Moschetti, M., Shapiro, N. & Yang, Y., 2007. Processing seismic ambient noise data to obtain reliable broadband surface wave dispersion measurements, *Geophys. J. Int.,* **169**(3), 1239–1260.

Brenguier, F., Campillo, M., Hadziioannou, C., Shapiro, N., Nadeau, R.M. & Larose, E., 2008a. Postseismic relaxation along the San Andreas fault at Parkfield from continuous seismological observations, *Science,* **321**(5895), 1478–1481.

Brenguier, F., Shapiro, N.M., Campillo, M., Ferrazzini, V., Duputel, Z., Coutant, O. & Nercessian, A., 2008b. Towards forecasting volcanic eruptions using seismic noise, *Nat. Geosci.,* **1**(2), 126.

Bromirski, P.D. & Duennebier, F.K., 2002. The near-coastal microseism spectrum: spatial and temporal wave climate relationships, *J. geophys. Res.,* **107**(B8), ESE–5, doi:10.1029/2001JB000265.

Burtin, A., Bollinger, L., Vergne, J., Cattin, R. & Nábělek, J., 2008. Spectral analysis of seismic noise induced by rivers: a new tool to monitor spatiotemporal changes in stream hydrodynamics, *J. geophys. Res.,* **113**(B5), doi:10.1029/2007JB005034.

Capon, J., 1973. Signal processing and frequency–wavenumber spectrum analysis for a large aperture seismic array, *Methods in Computational Physics*. (Elsevier, 1973), **13,** 1–59.

Cessaro, R.K., 1994. Sources of primary and secondary microseisms, *Bull. seism. Soc. Am.,* **84**(1), 142–148.

Chen, C., Gilbert, H., Andronicos, C., Hamburger, M.W., Larson, T., Marshak, S. & Yang, X., 2016. Shear velocity structure beneath the central United States: implications for the origin of the Illinois Basin and intraplate seismicity, *Geochem. Geophys. Geosyst.,* **17**(3), 1020–1041.

Cornou, C., Bard, P.Y. & Dietrich, M., 2003. Contribution of dense array analysis to the identification and quantification of basin-edge-induced waves, part II: application to Grenoble basin (French Alps), *Bull. seism. Soc. Am.,* **93**(6), 2624–2648.

Dart, R.L., 1992. Catalog of pre-Cretaceous geologic drill-hole data from the upper Mississippi embayment: a revision and update of open file report 90–260, USGS Technical Report, US Department of the Interior, US Geological Survey.

Dart, R.L. & Swolfs, H.S., 1998. Contour mapping of relic structures in the Precambrian basement of the Reelfoot rift, North American midcontinent, *Tectonics,* **17**(2), 235–249.

Derode, A., Larose, E., Campillo, M. & Fink, M., 2003. How to estimate the greens function of a heterogeneous medium between two passive sensors? Application to acoustic waves, *Appl. Phys. Lett.,* **83**(15), 3054–3056.

Dumouchel, W. & O'Brien, F., 1989. Integrating a robust option into a multiple regression computing environment, in *Computer Science and Statistics: Proceedings of the 21st Symposium on the Interface,* pp. 297–302, American Statistical Association, Alexandria, VA.

Duputel, Z., Ferrazzini, V., Brenguier, F., Shapiro, N., Campillo, M. & Nercessian, A., 2009. Real time monitoring of relative velocity changes using ambient seismic noise at the Piton de la Fournaise volcano (La Réunion) from January 2006 to June 2007, *J. Volc. Geotherm. Res.,* **184**(1–2), 164–173.

Field, E.H., 1996. Spectral amplification in a sediment-filled valley exhibiting clear basin-edge-induced waves, *Bull. seism. Soc. Am.,* **86**(4), 991–1005.

Fu, Y.V. & Li, A., 2015. Crustal shear wave velocity and radial anisotropy beneath the Rio Grande rift from ambient noise tomography, *J. geophys. Res.,* **120**(2), 1005–1019.

Furumura, M. & Sasatani, T., 1996. Secondarily generated surface waves in the Tokachi basin, Hokkaido, Japan, *J. Phys. Earth,* **44**(2), 115–132.

Gerstoft, P., Shearer, P.M., Harmon, N. & Zhang, J., 2008. Global P, PP, and PKP wave microseisms observed from distant storms, *Geophys. Res. Lett.,* **35**(23), doi:10.1029/2008GL036111.

Gu, Y.J. & Shen, L., 2012. Microseismic noise from large ice-covered lakes?, *Bull. seism. Soc. Am.,* **102**(3), 1155–1166.

Gu, Y.J., Dublanko, C., Lerner-Lam, A., Brzak, K. & Steckler, M., 2007. Probing the sources of ambient seismic noise near the coasts of southern Italy, *Geophys. Res. Lett.,* **34**(22), doi:10.1029/2007GL031967.

Hallier, S., Chaljub, E., Bouchon, M. & Sekiguchi, H., 2008. Revisiting the basin-edge effect at Kobe during the 1995 Hyogo-Ken Nanbu earthquake, *Pure appl. Geophys.,* **165**(9–10), 1751–1760.

Harmon, N., Rychert, C. & Gerstoft, P., 2010. Distribution of noise sources for seismic interferometry, *Geophys. J. Int.,* **183**(3), 1470–1484.

Hasselmann, K., 1963. A statistical analysis of the generation of microseisms, *Rev. Geophys.,* **1**(2), 177–210.

Hatayama, K., Matsunami, K., Iwata, T. & Irikura, K., 1995. Basin-induced love waves in the eastern part of the Osaka basin, *J. Phys. Earth,* **43**(2), 131–155.

Hildenbrand, T.G. & Hendricks, J.D., 1995. Geophysical setting of the Reelfoot rift and relations between rift structures and the New Madrid seismic zone. USGS Technical Report, No. 1538-E, US Geological Survey, doi:10.3133/pp1538E.

Hillers, G., Ben-Zion, Y., Campillo, M. & Zigone, D., 2015. Seasonal variations of seismic velocities in the San Jacinto fault area observed with ambient seismic noise, *Geophys. J. Int.,* **202**(2), 920–932.

Holland, P.W. & Welsch, R.E., 1977. Robust regression using iteratively reweighted least-squares, *Commun. Stat.: Theory Methods,* **A6,** 813–827.

Husker, A.L., Kohler, M.D. & Davis, P.M., 2006. Anomalous seismic amplitudes measured in the Los Angeles Basin interpreted as a basin-edge diffraction catastrophe, *Bull. seism. Soc. Am.,* **96**(1), 147–164.

Joyner, W.B., 2000. Strong motion from surface waves in deep sedimentary basins, *Bull. seism. Soc. Am.,* **90**(6B), S95–S112.

Kawase, H., 1996. The cause of the damage belt in Kobe: the basin-edge effect, constructive interference of the direct S-wave with the basin-induced diffracted/Rayleigh waves, *Seismol. Res. Lett.,* **67**(5), 25–34.

Kedar, S., Longuet-Higgins, M., Webb, F., Graham, N., Clayton, R. & Jones, C., 2008. The origin of deep ocean microseisms in the north Atlantic Ocean, *Proc. R. Soc. A,* **464**(2019), 777–793.

Kibblewhite, A.C. & Ewans, K.C., 1985. Wave–wave interactions, microseisms, and infrasonic ambient noise in the ocean, *J. acoust. Soc. Am.,* **78**(3), 981–994.

Landés, M., Hubans, F., Shapiro, N.M., Paul, A. & Campillo, M., 2010. Origin of deep ocean microseisms by using teleseismic body waves, *J. geophys. Res.,* **115**(B5), doi:10.1029/2009JB006918.

Langston, C.A., Bodin, P., Powell, C., Withers, M., Horton, S. & Mooney, W., 2005. Bulk sediment Q_p and Q_s in the Mississippi embayment, central United States, *Bull. seism. Soc. Am.,* **95**(6), 2162–2179.

Langston, C.A., Chiu, S.-C.C., Lawrence, Z., Bodin, P. & Horton, S., 2009. Array observations of microseismic noise and the nature of H/V in the Mississippi embayment, *Bull. seism. Soc. Am.,* **99**(5), 2893–2911.

Lecocq, T., Caudron, C. & Brenguier, F., 2014. MSNoise, a python package for monitoring seismic velocity changes using ambient seismic noise, *Seismol. Res. Lett.,* **85**(3), 715–726.

Liang, C. & Langston, C.A., 2008. Ambient seismic noise tomography and structure of eastern North America, *J. geophys. Res.,* **113**(B3), doi:10.1029/2007JB005350.

Liang, C. & Langston, C.A., 2009. Three-dimensional crustal structure of eastern North America extracted from ambient noise, *J. geophys. Res.,* **114**(B3), doi:10.1029/2008JB005919.

Lin, F.C., Ritzwoller, M.H., Townend, J., Bannister, S. & Savage, M.K., 2007. Ambient noise Rayleigh wave tomography of New Zealand, *Geophys. J. Int.,* **170**(2), 649–666.

Lin, F.C., Moschetti, M.P. & Ritzwoller, M.H., 2008. Surface wave tomography of the western United States from ambient seismic noise: Rayleigh and Love wave phase velocity maps, *Geophys. J. Int.,* **173**(1), 281–298.

Lin, F.-C., Li, D., Clayton, R.W. & Hollis, D., 2013. High-resolution 3D shallow crustal structure in Long Beach, California: application of ambient noise tomography on a dense seismic array noise tomography with a dense array, *Geophysics,* **78**(4), Q45–Q56.

Liu, C., Langston, C.A., Powell, C.A. & Cramer, C.H., 2018a. Near surface to upper mantle velocity structure in the Mississippi embayment from ambient noise tomography, AGUFM, 2018, S13C-0454.

Liu, C., Aslam, K.S. & Daub, E.G., 2020. Estimating seismic velocity variations in the Mississippi embayment from analysis of the ambient seismic field, doi:10.1002/essoar.10502143.1.

Liu, Z., Huang, J., He, P. & Qi, J., 2018b. Ambient noise monitoring of seismic velocity around the Longmen Shan fault zone from 10 years of continuous observation, *J. geophys. Res.,* **123**(10), 8979–8994.

Longuet-Higgins, M.S., 1950. A theory of the origin of microseisms, *Phil. Trans. R. Soc. A,* **243**(857), 1–35.

Meier, U., Shapiro, N.M. & Brenguier, F., 2010. Detecting seasonal variations in seismic velocities within Los Angeles basin from correlations of ambient seismic noise, *Geophys. J. Int.,* **181**(2), 985–996.

Nakata, N., Chang, J.P., Lawrence, J.F. & Boué, P., 2015. Body wave extraction and tomography at Long Beach, California, with ambient-noise interferometry, *J. geophys. Res.,* **120**(2), 1159–1173.

Narayan, J.P., 2012. Effects of P-wave and S-wave impedance contrast on the characteristics of basin transduced Rayleigh waves, *Pure appl. Geophys.,* **169**(4), 693–709.

Nawab, S., Dowla, F. & Lacoss, R., 1985. Direction determination of wideband signals, *IEEE Trans. Acoust. Speech Signal Process.,* **33,** 1114–1122.

Nishida, K., Montagner, J.P. & Kawakatsu, H., 2009. Global surface wave tomography using seismic hum, *Science,* **326**(5949), 112, doi:10.1126/science.1176389.

Niu, F., Silver, P.G., Daley, T.M., Cheng, X. & Majer, E.L., 2008. Preseismic velocity changes observed from active source monitoring at the Parkfield SAFOD drill site, *Nature,* **454**(7201), 204.

Reading, A.M., Koper, K.D., Gal, M., Graham, L.S., Tkalčić, H. & Hemer, M.A., 2014. Dominant seismic noise sources in the Southern Ocean and West Pacific, 2000–2012, recorded at the Warramunga Seismic Array, Australia, *Geophys. Res. Lett.,* **41**(10), 3455–3463.

Retailleau, L., Boué, P., Stehly, L. & Campillo, M., 2017. Locating microseism sources using spurious arrivals in intercontinental noise correlations, *J. geophys. Res.,* **122**(10), 8107–8120.

Ritzwoller, M.H., Shapiro, N.M., Barmin, M.P. & Levshin, A.L., 2002. Global surface wave diffraction tomography, *J. geophys. Res.,* **107**(B12), doi:10.1029/2002JB001777.

Rovelli, A., Scognamiglio, L., Marra, F. & Caserta, A., 2001. Edge-diffracted 1-sec surface waves observed in a small-size intramountain basin (Colfiorito, Central Italy), *Bull. seism. Soc. Am.,* **91**(6), 1851–1866.

Seber, G.A.F. & Wild, C.J., 2003. *Nonlinear Regression,* Wiley-Interscience, http://site.ebrary.com/id/10275079.

Sens-Schönfelder, C. & Wegler, U., 2006. Passive image interferometry and seasonal variations of seismic velocities at Merapi volcano, Indonesia, *Geophys. Res. Lett.,* **33**(21), doi:10.1029/2006GL027797.

Shapiro, N.M., Ritzwoller, M. & Bensen, G., 2006. Source location of the 26 sec microseism from cross-correlations of ambient seismic noise, *Geophys. Res. Lett.,* **33**(18), doi:10.1029/2006GL027010.

Silver, P.G., Daley, T.M., Niu, F. & Majer, E.L., 2007. Active source monitoring of cross-well seismic travel time for stress-induced changes, *Bull. seism. Soc. Am.,* **97**(1B), 281–293.

Snieder, R., 2004. Extracting the greens function from the correlation of coda waves: a derivation based on stationary phase, *Phys. Rev. E,* **69**(4), 046610, doi:10.1103/PhysRevE.69.046610.

Stehly, L., Campillo, M. & Shapiro, N., 2006. A study of the seismic noise from its long-range correlation properties, *J. geophys. Res.,* **111**(B10), doi:10.1029/2005JB004237.

Tian, Y. & Ritzwoller, M.H., 2015. Directionality of ambient noise on the Juan de Fuca plate: implications for source locations of the primary and secondary microseisms, *Geophys. J. Int.,* **201**(1), 429–443.

Tsai, V.C., 2009. On establishing the accuracy of noise tomography travel-time measurements in a realistic medium, *Geophys. J. Int.,* **178**(3), 1555–1564.

Wapenaar, K., 2004. Retrieving the elastodynamic Green's function of an arbitrary inhomogeneous medium by cross correlation, *Phys. Rev. Lett.,* **93**(25), 254301, doi:10.1103/PhysRevLett.93.254301.

Weaver, R., Froment, B. & Campillo, M., 2009. On the correlation of non-isotropically distributed ballistic scalar diffuse waves, *J. acoust. Soc. Am.,* **126**(4), 1817–1826.

Weaver, R.L. & Lobkis, O.I., 2001. Ultrasonics without a source: thermal fluctuation correlations at MHz frequencies, *Phys. Rev. Lett.,* **87**(13), 134301, doi:10.1103/PhysRevLett.87.134301.

Wiechert, E., 1904. Discussion, verhandlung der zweiten internationalen seismologischen konferenz, *Beitrage Zur Geophys.,* **2,** 41–43.

Wu, C., Delorey, A., Brenguier, F., Hadziioannou, C., Daub, E.G. & Johnson, P., 2016. Constraining depth range of S wave velocity decrease after large earthquakes near Parkfield, California, *Geophys. Res. Lett.,* **43**(12), 6129–6136.

Yang, Y. & Ritzwoller, M.H., 2008. Characteristics of ambient seismic noise as a source for surface wave tomography, *Geochem. Geophys. Geosyst.,* **9**(2), doi:10.1029/2007GC001814.

Yao, H. & Van Der Hilst, R.D., 2009. Analysis of ambient noise energy distribution and phase velocity bias in ambient noise tomography, with application to SE Tibet, *Geophys. J. Int.,* **179**(2), 1113–1132.

Yao, H., van Der Hilst, R.D. & De Hoop, M.V., 2006. Surface-wave array tomography in SE Tibet from ambient seismic noise and two-station analysis: I-phase velocity maps, *Geophys. J. Int.,* **166**(2), 732–744.

Young, I., 1999. Seasonal variability of the global ocean wind and wave climate, *Int. J. Climatol.,* **19**(9), 931–950.

Zeng, X. & Ni, S., 2010. A persistent localized microseismic source near the Kyushu Island, Japan, *Geophys. Res. Lett.,* **37**(24), doi:10.1029/2010GL045774.

SUPPORTING INFORMATION

Supplementary data are available at *GJI* online.

Figure S1. Amplitude of signals (red circles) and noise (blue circles) for 5000 measurements. The amplitude of signal is 10 times greater than that of noise. The standard deviation of noise is 1.5×10^{-5}.

Figure S2. Station pairs within 100 km (black) and station pairs observing sedimentary Rayleigh (left, coloured) and Love (right, coloured) waves. Station pairs observing sedimentary surface waves are well in the interior of the ME.

Figure S3. Group velocity dispersion curves for sedimentary Rayleigh (a) and Love (b) waves. The dominant period range is 1–5 s.

Figure S4. 2-D frequency–wavenumber analysis of monthly time-series in the passband of 0.2–1 Hz. The major energy arrival with slowness of 0.3 s km^{-1} in March might be a crustal surface wave. The slowness for low-velocity sedimentary surface wave ranges from 0.5 to 1 s km^{-1}.

Please note: Oxford University Press is not responsible for the content or functionality of any supporting materials supplied by the authors. Any queries (other than missing material) should be directed to the corresponding author for the paper.